ADVANCED MATERIALS
www.advmat.de

Bilayer Zwitterionic Metal-Organic Framework for Selective All-Solid-State Superionic Conduction in Lithium Metal Batteries

Yuan Ouyang, Wei Gong, Qi Zhang, Jia Wang, Sijia Guo, Yingbo Xiao, Dixiong Li, Changhong Wang, Xueliang Sun, Chaoyang Wang,* and Shaoming Huang**

Solid-state batteries (SSBs) hold immense potential for improved energy density and safety compared to traditional batteries. However, existing solid-state electrolytes (SSEs) face challenges in meeting the complex operational requirements of SSBs. This study introduces a novel approach to address this issue by developing a metal-organic framework (MOF) with customized bilayer zwitterionic nanochannels (MOF-BZN) as high-performance SSEs. The BZN consist of a rigid anionic MOF channel with chemically grafted soft multicationic oligomers (MCOs) on the pore wall. This design enables selective superionic conduction, with MCOs restricting the movement of anions while coulombic interaction between MCOs and anionic framework promoting the dissociation of Li^+. MOF-BZN exhibits remarkable Li^+ conductivity (8.76×10^{-4} S cm^{-1}), high Li^+ transference number (0.75), and a wide electrochemical window of up to 4.9 V at 30 °C. Ultimately, the SSB utilizing flame retarded MOF-BZN achieves an impressive specific energy of 419.6 Wh $kg_{anode+cathode+electrolyte}^{-1}$ under constrained conditions of high cathode loading (20.1 mg cm^{-2}) and limited lithium metal source. The constructed bilayer zwitterionic MOFs present a pioneering strategy for developing advanced SSEs for highly efficient SSBs.

1. Introduction

Solid-state batteries (SSBs) utilizing lithium metal as the anode have gained significant attention as promising energy storage devices, offering higher energy density and improved safety compared to liquid counterparts.[1–5] To achieve high-performance SSBs, the development of advanced solid-state electrolytes (SSEs) is crucial.[6–8] Conventional SSEs, mainly including solid inorganic electrolytes (SIEs) and solid polymeric electrolytes (SPEs), have been extensively investigated.[9–13] However, these conventional SSEs fail to meet the diverse demand of SSBs. SIEs generally exhibit high ionic conductivity, but they lack sufficient stability, machinability, and interfacial compatibility with electrodes. For instance, sulfide-based SSEs suffer from poor air stability, while oxide SSEs like $Li_7La_3Zr_2O_{12}$ (LLZO) face challenges in achieving suitable thickness, especially for pouch cell applications.[14–17] SPEs offer better processability and interfacial resistance compared to SIEs, but they are limited by their relatively low ionic conductivity (typically 10^{-8}-10^{-5} S cm^{-1} at room temperature) and low ion transference number (often < 0.3) due to the coupling of ion transport with segmental dynamics. Although composite SSEs provide a compromise, they inevitably involve trade-offs between ionic conductivity, ion selectivity, and interfacial contact. Thus, there is a high demand for innovative strategies to develop advanced SSEs with excellent overall properties.

Porous materials such as metal-organic frameworks (MOFs) offer distinct advantages as artificial channels for ionic conduction due to their tunable pore structure and chemical environment.[18–21] Presently, only semisolid state MOFs incorporating electrolyte solvents like propylene carbonate (PC) achieve room temperature conductivity exceeding 10^{-4} S cm^{-1}. However, these systems are flammable and prone to side reactions.[10] All-solid-state MOF-based electrolytes (MOF SSEs) typically exhibit intrinsic ionic conductivities below 10^{-5} S cm^{-1}, which falls short of the requirements for safe operation in high-energy SSBs. The inadequate Li^+ conductivity in MOF SSEs can be attributed to both the sparse hopping sites (such as —OH, —SO_3H, —COOH and —NH_2) decorating the pore walls and the strong binding of

Y. Ouyang, W. Gong, Q. Zhang, J. Wang, S. Guo, Y. Xiao, D. Li, S. Huang
Guangzhou Key Laboratory of Low-Dimensional Materials and Energy Storage Devices
Guangdong University of Technology
Guangzhou 510006, China
E-mail: qzhangmse@gdut.edu.cn; smhuang@gdut.edu.cn
C. Wang
Electrochemical Engine Center (ECEC) and Department of Mechanical Engineering
Pennsylvania State University
University Park, PA USA
E-mail: cxw31@psu.edu
C. Wang, X. Sun
Department of Mechanical and Materials Engineering
University of Western Ontario
1151 Richmond St., London, ON N6A 3K7, Canada
S. Huang
College of Materials
Chemistry and Chemical Engineering
Hangzhou Normal University
No. 2318 Yuhangtang Rd., Cangqian, Yuhang District, Hangzhou China
The ORCID identification number(s) for the author(s) of this article can be found under https://doi.org/10.1002/adma.202304685

DOI: 10.1002/adma.202304685

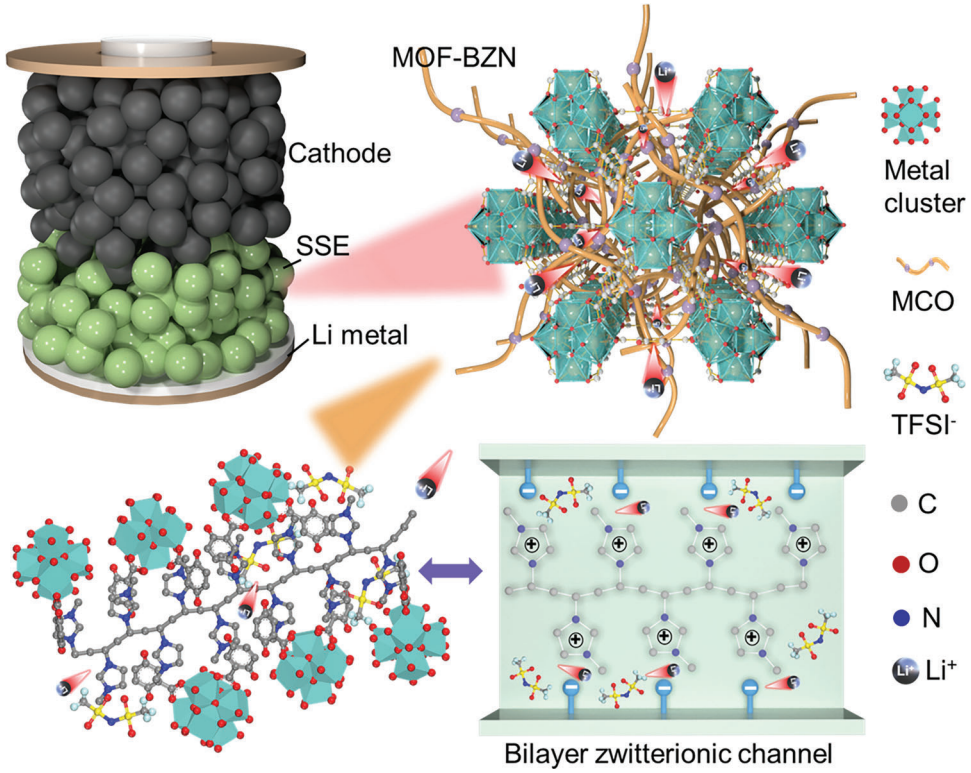

Figure 1. Design strategy of metal-organic framework (MOF) solid-state electrolyte (SSE) with bilayer zwitterionic nanochannels (BZN).

Li^+ to these polar adsorption sites. The former results in long hopping distances, while the latter increases the energy required for Li^+ dissociation from the coordinated state, creating a high energy barrier for Li^+ transport within MOF nanochannels.

Herein, we present a novel MOF-based SSE that incorporates bilayer zwitterionic nanochannels (BZNs) to enable efficient and selective ion transport in SSBs. The framework, named MOF-BZN, is constructed by grafting soft multicationic oligomers (MCOs) onto the channels of a rigid anionic MOF framework. Through chemical immobilization and nanoconfinement effects, the dynamics of MCOs are effectively suppressed, allowing for the decoupling of ion transport from MCO relaxation. Moreover, the competing interaction between cationic MCOs and negative adsorption sites in MOF-BZN promotes the dissociation of Li^+ from the binding state, while the migration of anions is restricted due to charge interactions. Consequently, the immobilized MCOs extending from the pore walls act as ion-selective gates that facilitate the transport of only Li^+ (**Figure 1**).

Finally, MOF-BZN demonstrates a high ionic conductivity of 8.76×10^{-4} S cm^{-1} at room temperature, which is approximately 300 times higher than that of traditional all-solid-state MOFs. Additionally, it exhibits an excellent lithium ion transference number ($t_{Li}{}^+$) of 0.75, exceptional chemical stability (4.9 V), high thermostability, and flame retardance. Importantly, MOF-BZN enables the safe operation of solid-state full cells, achieving a high specific energy of 419.6 Wh $kg_{\text{anode+cathode+electrolyte}}{}^{-1}$ under high-loading $LiNi_{0.8}Mn_{0.1}Co_{0.1}O_2$ (NCM-811) cathode (20.1 mg cm^{-2}) and controlled N/P ratio (2.4).

2. Results and Discussion

2.1. Material Synthesis and Structural Analysis

As indicated in **Figure 2**a, MOF-OH-V, a multivariable and bifunctional UiO (UiO is short for University of Oslo) type MOF, was firstly designed and constructed with 2-vinylterephthalic acid and 2,5-dihydroxyterephthalic acid. In the framework, the vinyl will be used for the subsequent copolymerization with allyl functionalized cationic monomers and the –OH groups are designed to regulate the chemical interaction within channels. For comparison, UiO-66-V and UiO-66-2OH with single functional group were synthesized as well (denoted later as MOF-V and MOF-2OH, Figure S1, Supporting Information). The powder X-ray diffractometry (PXRD) patterns in Figure S2 (Supporting Information) indicate that the synthesized MOFs are isostructural to UiO-66. Moreover, they have a similar particle size of around 200–500 nm (Figure S3, Supporting Information). The molecular ratio of ligands in MOF-OH-V is determined to be around 1:1 by the solution nuclear magnetic resonance (NMR) in Figure S4 (Supporting Information).

The highly-conductive Li-IL molecule containing LiTFSI and [AMIM][TFSI], where AMIM is 1-allyl-3-methylimidazolium and $TFSI^-$ is bis(trifluoromethylsulfonyl)imide, was herein designed and synthesized as the monomer (Figure S5, Supporting Information). Excess Li-IL was mixed with MOFs (MOF-OH-V and MOF-V) and encapsulated into the pores by siphon effect with the assistance of vacuum to conduct the nanoconfined in situ copolymerization. The nanoconfinement effect is hopeful to generate

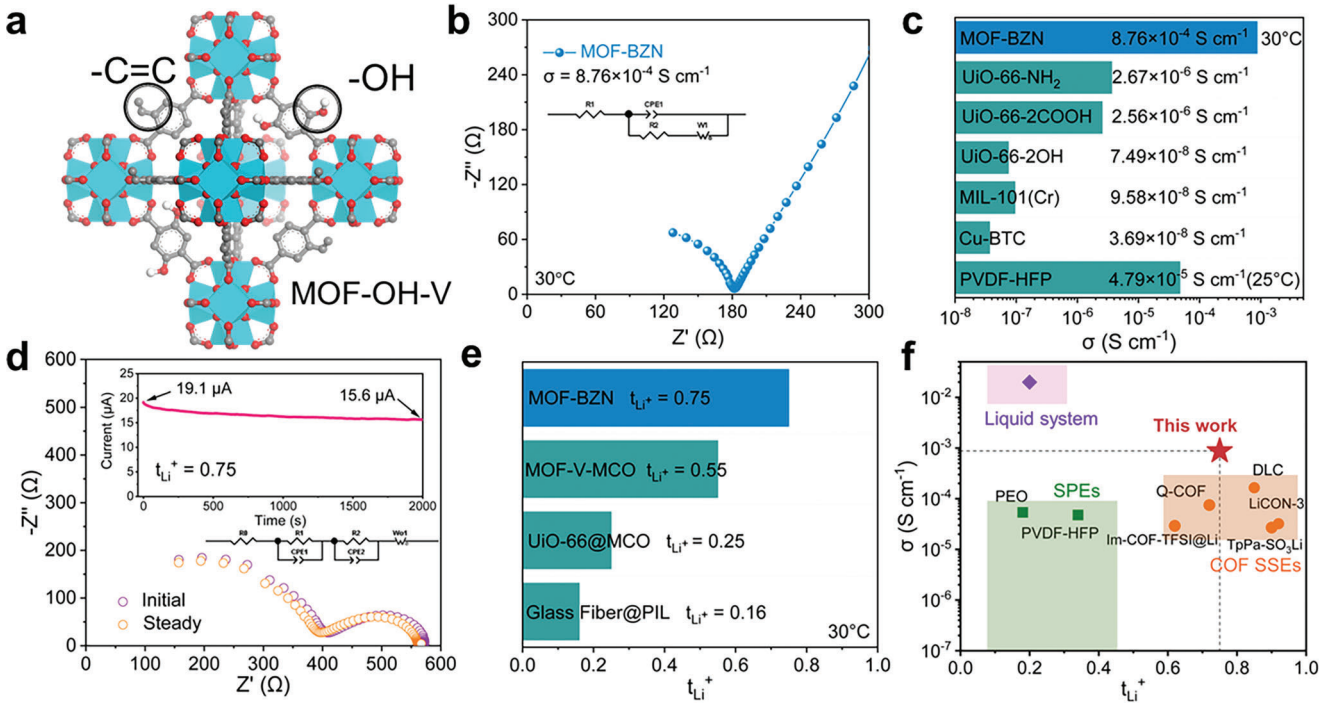

Figure 2. Li^+ transport performance of metal-organic framework (MOF) with customized bilayer zwitterionic nanochannels (MOF-BZN) ion conductors. a) Structural illustration of MOF-OH-V. b) Electrochemical impedance spectroscopy (EIS) spectrum of MOF-BZN at 30 °C. The inset is the equivalent circuit used for fitting impedance spectrum. c) Comparison of the Li^+ conductivity of MOF-BZN with other all-solid-state MOF conductors. d) EIS spectra before and after polarization of Li|MOF-BZN|Li cell, the insets show the corresponding polarization curve and the equivalent circuit used for fitting impedance spectra. e) Comparison of the t_{Li}^+ transference number of different electrolytes. f) Comparison of ion transport performance for different solid-state electrolyte (SSEs).

short multicationic molecular chains., i.e., MCOs. After washing out the free polymerized molecular chains, solid-state ion conductors, i.e., MOF-OH-V-MCO (denoted as MOF-BZN) and MOF-V-MCO can be achieved. The PXRD patterns and SEM images of MOFs after copolymerization in Figure S6 and S7 (Supporting Information) show that the MOFs remain intact during the copolymerization reaction.

The existence of generated MCOs was firstly characterized by matrix-assisted laser desorption/ionization time-of-flight (MALDI-TOF) mass spectrometry. As can be seen in Figure S8 (Supporting Information), the calculated number of monomers in MCOs of MOF-BZN distributes from 12 to 32, much lower than that in the polymerized Li-IL (PIL) without MOF (214 to 234) (Figure S9, Supporting Information), indicating the nanoconfinement effect of MOF on polymerization of IL monomers. These shorter MCOs immobilized in MOF pores are expected to enhance the Li^+ transport in channels.

In the Fourier transform infrared (FT-IR) spectra, the peaks at around 1190 and 1050 cm^{-1}, which represent the characteristic bands of imidazolium ring, indicate the existence of MCOs in the pores of MOFs (Figure S10, Supporting Information). Moreover, the high-resolution ^{13}C solid-state magic-angle sample-spinning NMR (CP/MAS ^{13}C NMR) spectra of vinyl functionalized MOF before and after copolymerization in Figure S11 (Supporting Information) show that the C signal belonging to vinyl disappeared after copolymerization, suggesting the chemical reaction and bonding between the vinyl groups in framework and MCOs. Furthermore, the Brunauer–Emmett–Teller (BET) specific surface areas calculated from the N_2 adsorption–desorption isotherms in Figure S12 (Supporting Information) confirm that, the specific surface areas of MOF-BZN (2.2 $m^2\ g^{-1}$) and MOF-V-MCO (1.8 $m^2\ g^{-1}$) decrease drastically compared with that of MOF-OH-V (506.9 $m^2\ g^{-1}$) and MOF-V (881.0 $m^2\ g^{-1}$), which can be attributed to the chemically grafted MCOs in pores.

The chemical anchoring of MCOs with vinyl groups in MOF can also be verified by the impact of copolymerization on the states of MCOs. As shown in Figure S13 (Supporting Information), different from the solid-state MOF-BZN, the PIL remains liquid because of its low degree of polymerization. MOF-2OH without vinyl groups was also applied to conduct the nanoconfined polymerization to study the impact of vinyl. Without vinyl groups, it is supposed that the Li-IL monomers experienced "self" polymerization within the pores of MOF-2OH. As a result, the surface of pressed MOF-2OH@MCO pellet exhibits liquid-state, indicating that the MCO remains liquid in the pores of MOF-2OH (Figure S14, Supporting Information). By contrast, both the powders and the pressed pellet of MOF-BZN exhibit solid-state, which can be ascribed to the immobilization of most MCOs within the channels and is consistent with the results of CP/MAS ^{13}C NMR spectra (Figure S11, Supporting Information). The former results demonstrate that a MOF-BZN with bilayer zwitterionic channels was successfully developed, which contains both the –OH functionalized rigid anionic framework and the nonhomogeneous MCOs extended from pore wall into channels.

2.2. Li^+ Conduction in MOF-BZN

The actual ionic conductivities of synthesized MOF were investigated by collecting the electrochemical impedance spectroscopy (EIS) spectra in the temperature range from −20 °C to 60 °C (Figure S15, Supporting Information). As exhibited in Figure 2b, the solid-state MOF-BZN possesses an ionic conductivity of 8.76 × 10^{-4} S cm^{-1} at 30 °C. The ionic conductivity increases as the increasing of temperature and the activation energy (E_a) for ion diffusion in MOF-BZN calculated from Figure S16 (Supporting Information) is 0.54 eV. For comparison, the intrinsic ionic conductivities of different MOFs without electrolyte solvent in pores were evaluated under the same conditions and are summarized in Figure 2c and Figure S17 (Supporting Information). Without the assistance of liquid electrolyte or Li-IL in pores, most all-solid-state MOFs conductors output ionic conductivities in the range from 10^{-8} to 10^{-6} S cm^{-1} at room temperature, comparable to the intrinsic ionic conductivities of classical SPEs such as poly(vinylidene fluoride-hexafluoropropylene) (PVDF-HFP).[22] Therefore, the ionic conductivity of MOF-BZN is almost 300 times higher than the average of traditional MOF electrolytes.

As both positive and negative ions can migrate under electric field, $t_{Li}{}^+$ was then investigated to evaluate the proportion of ionic conductivity contributed by the Li^+ migration. To study the impact of different functional groups on the transference number, Glass Fiber@PIL, UiO-66@MCO and MOF-V-MCO were synthesized and investigated. As shown in Figure S18a,b (Supporting Information), the $t_{Li}{}^+$ of PIL and synthesized UiO-66@MCO are calculated to be as low as 0.16 and 0.25, respectively, which agrees with the reported results of Li-IL.[23] The low $t_{Li}{}^+$ indicates that ions transport is coupled with segmental motion in these two systems. By sharp contrast, MOF-V-MCO shows a $t_{Li}{}^+$ of 0.55 (Figure S18c, Supporting Information), implying that the chemical immobilization of MCOs can greatly restrain the migration of $TFSI^-$. With bilayer zwitterionic channels, MOF-BZN exhibits a higher $t_{Li}{}^+$ of 0.75 than MOF-V-MCO (Figure 2d,e), verifying the combination of chemical immobilization and chemical interaction can effectively decouple Li^+ transport with relaxation of MCOs and meanwhile restrain movement of $TFSI^-$.

According to the aforementioned results, MOF-BZN exhibits outstanding comprehensive electrochemical properties. As compared in Figure 2f and Table S1 (Supporting Information), MOF-BZN offers higher ionic conductivity than most reported SIEs including $Li_{1.3}Al_{0.3}Ti_{1.7}(PO_4)_3$ (LATP) (7.0 × 10^{-4} S cm^{-1}) and LLZO (2.4 × 10^{-4} S cm^{-1}), and notably superior to that of the solid-state SPEs such as polyethylene oxide (PEO) (5.4 × 10^{-5} S cm^{-1}), PVDF-HFP (1.73 × 10^{-5} S cm^{-1}), and newly emerged covalent-organic frameworks (COFs) at 30 °C.,[3,22,24–33] In terms of $t_{Li}{}^+$, MOF-BZN also achieves much higher performance than SPEs and liquid system. All in all, the solid-state MOF-BZN conductor with both high ionic conductivity and improved ion transference number is achieved.

The local chemical environments and dynamics of Li^+ were further investigated using ^7Li solid-state NMR (ss-NMR) spectroscopy to understand the origin of the enhanced Li^+ conductivity. As indicated in **Figure 3**a, a broad signal was observed in the spectrum of dry MOF-OH-V, indicating the stronger bound state and the less movability of Li^+ in corresponding channels. By sharp contrast, the Li^+ signal gets sharped in the spectrum of MOF-BZN. Specifically, the ^7Li full-width at half-maximum for MOF-OH-V is 608.5 Hz, however it decreases to 130.0 Hz for MOF-BZN, demonstrating the easier dissociation of Li^+ from coordinated state in the channels of MOF-BZN.

The aforementioned results can also be verified by theoretical calculations. Molecular dynamics (MD) simulations were applied to give an insight into the chemical interaction and diffusion kinetics of ions in different MOF channels. The MOF-BZN SSE model was constructed by anchoring MCOs onto the vinyl groups in MOF-OH-V. Figure 3b and Figure S19 (Supporting Information) indicate that the binding energy for Li^+ in MOF-2OH (64.2 kcal mol^{-1}) is higher than that in MOF-BZN (60.9 kcal mol^{-1}) with introduced MCOs, suggesting that Li^+ can be more easily released during transport in the MOF-BZN channels.

The higher mobility of Li^+ can also be corroborated through the calculated radial distribution functions (RDFs(r)) in Figure 3c. The dominating peak of RDF(r) for Li–O (hydroxy) in MOF-OH-V appears at around 1.8 Å, which is similar to that of LiTFSI, indicating the strong coordination between Li^+ and the –OH in MOF pore walls. In MOF-BZN, the dominating RDF peak for Li–O locates at around 2.3 Å, implying the easier dissociation of Li^+ in MOF-BZN. Moreover, the dominating peak of RDF(r) for Li–N in LiTFSI appears at 1.9 Å, while it appears at 2.0 Å in MOF-BZN. These results match well with the sharped spectrum of ^7Li signal in MOF-BZN (Figure 3a) and indicate that the constraint toward Li^+ from the circumjacent chemical environment is weaker in MOF-BZN, which can be ascribed to the interaction between the negatively charged hydroxy in framework and positively charged MCOs within channels. As a result, MOF-BZN delivers a remarkably enhanced Li^+ diffusion behavior with an improved diffusion coefficient of 4.95 × 10^{-7} cm^2 s^{-1} than that in MOF-2OH (3.18 × 10^{-9} cm^2 s^{-1}) in the time evolution of the mean square displacement (MSD) in Figure 3d.

The chemical interaction and motion of anions were studied through MD calculation as well to understand the higher Li^+ transference number of MOF-BZN. Figure 3b shows that $TFSI^-$ suffer from a much higher binding energy of 109.6 kcal mol^{-1} in MOF-BZN than Li^+ (60.9 kcal mol^{-1}), suggesting the more difficult motion of $TFSI^-$ than Li^+. Moreover, the time evolution of the MSD in Figure 3e also indicates that the diffusion coefficient of $TFSI^-$ in MOF-BZN drastically decreases from 1.04 × 10^{-7} cm^2 s^{-1} in IL to 5.76 × 10^{-9} cm^2 s^{-1}, much lower than that of Li^+ (0.11). These results echo with the significantly improved transference number of MOF-BZN.

The ion transport models in different MOFs ion conductors are illustrated in Figure S20a,b (Supporting Information) and Figure 3f. Some neat MOF channels functionalized with chemical groups such as $–NH_2$ and –OH can realize single ion transport, which are however limited by inferior ionic conduction by the insufficient functional sites on the pore wall (Figure S20a, Supporting Information). In semisolid MOFs encapsulated with liquid-phase Li-IL, both Li^+ and anions can transport through the IL, thus leading to a low $t_{Li}{}^+$ (Figure S20b, Supporting Information). As illustrated in Figure 3f, MOF-BZN possesses multiply engineered channels functionalized with bilayer zwitterionic networks. The —OH groups and MCOs/$TFSI^-$ ion pairs provide sufficient hopping sites for Li^+ together, and meanwhile their mutual charge interaction delivers easier Li^+ dissociation. More

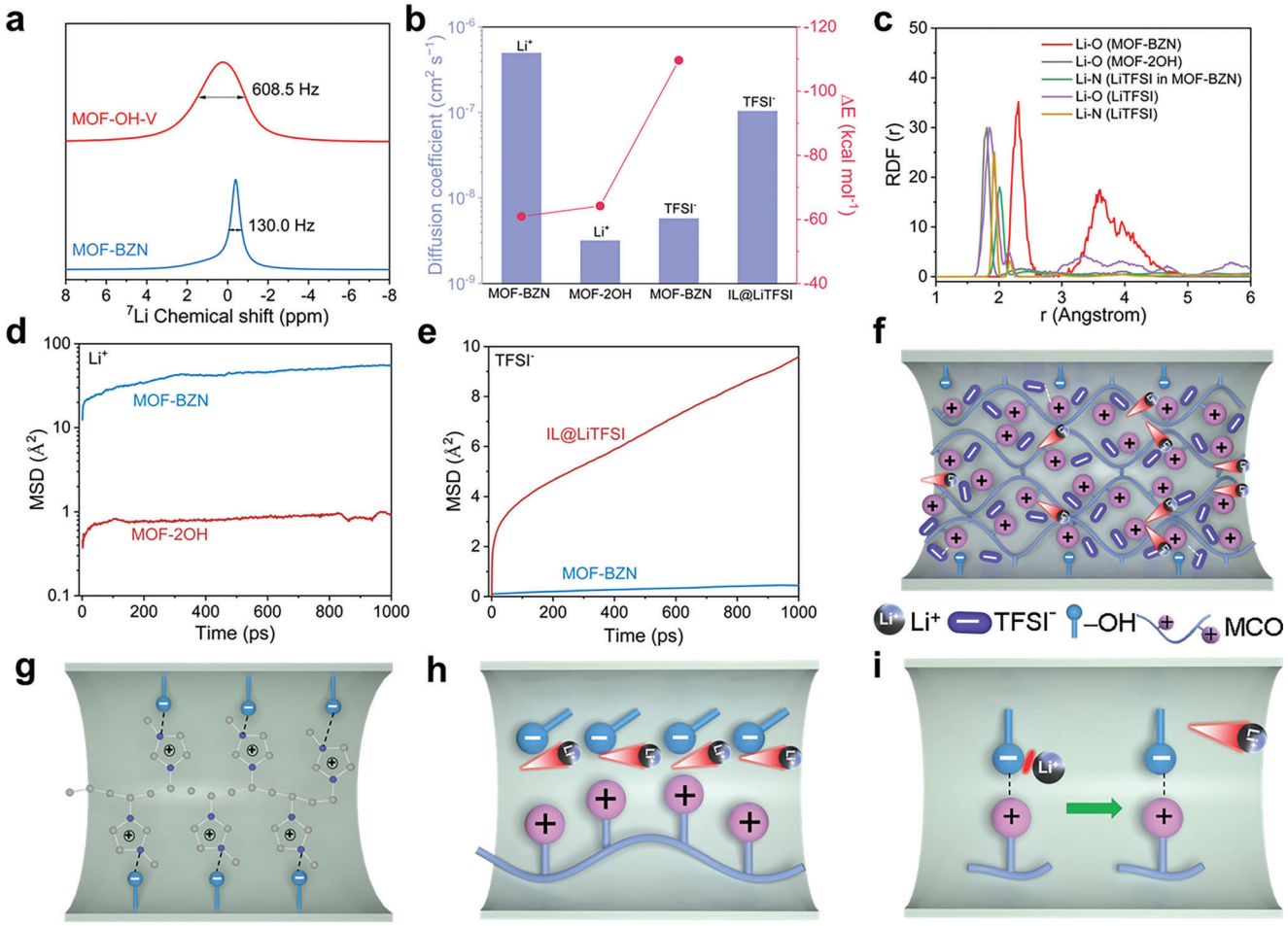

Figure 3. Ion conductivity and transport mechanism in metal-organic framework with customized bilayer zwitterionic nanochannels (MOF-BZN). a) 1D ^{7}Li nuclear magnetic resonance (NMR) of MOF-OH-V and MOF-BZN. b) Comparison of diffusion coefficient and binding energies for Li^+ and $TFSI^-$ in MOF-BZN, MOF-2OH and IL@LiTFSI. c) Calculated radial distribution functions (RDFs) of MOF-BZN, MOF-OH-V, and LiTFSI. Calculated mean square displacement (MSD) of Li^+ (d) and $TFSI^-$ (e) as a function of the simulation time. f) Schematic illustration of ion transport inside channels of MOF-BZN. g) The frustrated MCOs in anionic MOF channel. h) Sufficient hopping sites for Li^+ transport. i) Mechanism of promoted Li^+ dissociation in MOF-BZN.

importantly, different from the ions transport depending on segmental motion in traditional PILs and SPEs, independent Li^+ transport in MOF-BZN can be realized through ions hopping because of the frustrated MCOs (Figure 3g,h). As the dissociation of Li^+ is promoted while the motion of anions is restricted by charge interaction, high ionic conductivity and transference number are rendered simultaneously (Figure 3i).

2.3. SSE Membrane and Demonstration in Batteries

There is no doubt that, MOF-BZN possesses outstanding comprehensive electrochemical properties. Based on these inspiring results, a flexible SSE membrane with thickness of 42.9 µm and mass density of 7.6 mg cm^{-2} was further manufactured using MOF-BZN and 1 wt% polytetrafluoroethylene (PTFE) (**Figure 4**a,b), in which MOF-BZN was uniformly distributed (Figure S21, Supporting Information). The weight and thickness of commercial LATP SSE were investigated for comparison. Although the LATP SSE exhibits a comparable ionic conductivity of 7.0×10^{-4} S cm^{-1}, it has a much higher area mass density of 70.7 mg cm^{-2} and thickness of 260.0 µm (Figure 4c and Figure S22a, Supporting Information).[34] More importantly, such inorganic SSE is in the shape of pellet with a diameter of 11.9 mm, which is difficult to be manufactured into a larger size (Figure S22b, Supporting Information). While the mass density and thickness of MOF-BZN SSE membrane can be further optimized by improving the processing technology.

The electrochemical window of the MOF-BZN SSE was investigated by linear sweep voltammetry (LSV) test using a Li|SSE|SS (SS is short for stainless steel) cell at room temperature. As shown in Figure 4d, the electrochemical window of MOF-BZN SSE is 4.93 V (versus Li/Li^+), much wider than that of PIL (4.03 V) and PVDF-HFP (4.20 V).[32] Such high electrochemical stability of MOF-BZN SSE guarantees its application in SSBs with Li metal anode and different cathodes such as $LiFePO_4$ (LFP) and NCM-811. Chemical stability is crucial for practical application as well. For sulfide SSEs and oxide SSEs in air, not only their

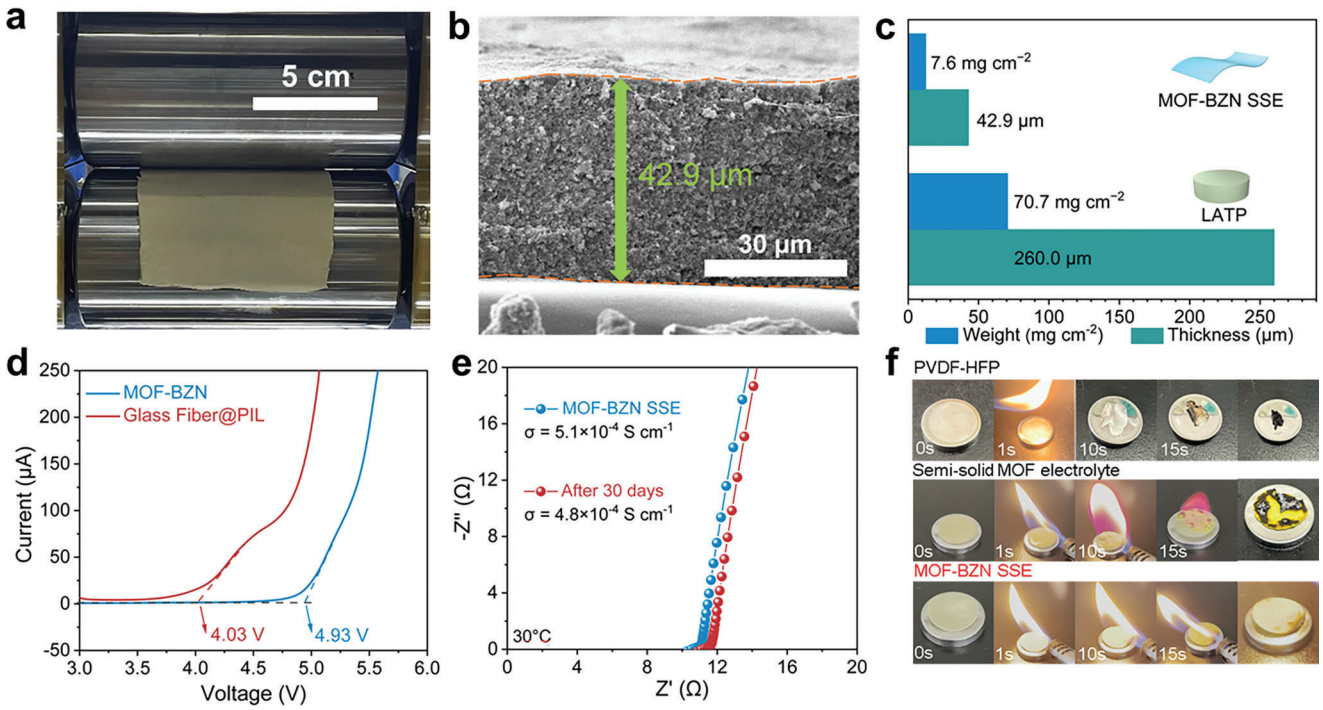

Figure 4. Characterizations of metal-organic framework with customized bilayer zwitterionic nanochannels (MOF-BZN) solid-state electrolyte (SSE) membrane. a) Digital photo of the MOF-BZN SSE membrane after hot calendaring. b) Cross-sectional SEM image of MOF-BZN SSE. c) Comparison of the thicknesses and qualities of MOF-BZN SSE membrane and commercial $Li_{1.3}Al_{0.3}Ti_{1.7}(PO_4)_3$ (LATP). d) Linear sweep voltammetry (LSV) of MOF-BZN SSE and Glass Fiber@PIL measured at 0.1 mV s^{-1}. e) Electrochemical impedance spectroscopy (EIS) spectra of MOF-BZN SSE before and after being exposed in air for 30 days. f) Flammability test of poly(vinylidene fluoride-hexafluoropropylene) (PVDF-HFP) electrolyte, semisolid MOF, and MOF-BZN SSE (This work).

reactivity can cause the drastic decrease of ionic conductivity, but also sulfide SSEs can produce toxic H_2S.[35,36] In contrast, MOF-BZN SSE with a high conductivity of 5.1×10^{-4} S cm^{-1} can remain intact and hold a high ionic conductivity of 4.8×10^{-4} S cm^{-1} and 4.7×10^{-4} S cm^{-1} after being exposed in air for over 30 days or being bended for over 50 times, respectively (Figure 4e and Figures S23, S24, Supporting Information), indicating its superior physical and chemical stability.

To address the safety issue of SSBs, the thermal stability of the SSE membrane was also evaluated. As shown in Figure S25 (Supporting Information), after being heated at 150 °C for 3 h, the commercial Celgard separator and PVDF-HFP membrane curled up and contracted. The Celgard separator burnt out after being heated at 300 °C for 3 h, whereas, the MOF-BZN SSE membrane remained almost unchanged, which can be ascribed to the good thermal stability of MOF particles (Figure S26, Supporting Information). Moreover, the MOF-BZN SSE membrane has excellent flame resistance (Figure 4f). The PVDF-HFP electrolyte, the conventional semisolid MOF electrolyte containing liquid organics in pores and solid-state MOF membrane can be ignited easily (Figure S27, Supporting Information). In stark contrast, the MOF-BZN SSE membrane is completely nonflammable, owing to the polymerized MCOs in pores.

Figure S28a,b, Supporting Information, elaborate the main challenges of different types of electrolytes for application in Li metal batteries (LMBs). As can be seen, although liquid electrolyte has higher Li^+ conductivity, the inevitable dendrite growth and flammability at high temperature (Figure 4f) have induced tough safety risks. Typical SIEs such as LATP possess high ionic conductivity and are flame retardant, but their poor interfacial compatibility with electrodes impedes the SSB performance.[37] SPEs are inferior in Li^+ conductivity and t_{Li}^+ at room temperature, and are inefficient in suppressing dendrite formation, leading to SSBs only work properly at elevated temperature (normally over 60 °C).[38,39] Speaking of semisolid MOF and COF electrolytes which have been intensively studied in recent years, they have shown talent in single ion transport and suppressing dendrite formation, however, most of them are posed to the safety issues because of the encapsulated liquid electrolyte in channels.

The interfacial resistances with electrodes were also evaluated by assembling Li|MOF SSE|Li symmetric cells (Figure S29, Supporting Information). MOF-BZN delivers a drastically decreased interfacial resistance compared with that of MOF-2OH, demonstrating that the extended longer MCOs on MOF surfaces can benefit ions transport among MOFs and at interfaces between MOF and Li metal. Moreover, MOF-BZN SSE membrane enables a stable Li plating/stripping (0.2 mA cm^{-2}) for over 400 h in a Li|SSE|Li symmetric cell, superior to the comparable Glass Fiber@PIL that induces rapidly rising polarization at 71 h (Figure S30, Supporting Information). This result verifies that MOF-BZN SSE membrane has good interfacial compatibility with Li metal and ability in suppressing lithium dendrites. Together with its improved safety compared with the liquid and quasi-solid electrolyte, it can be concluded that such SSE meets the various

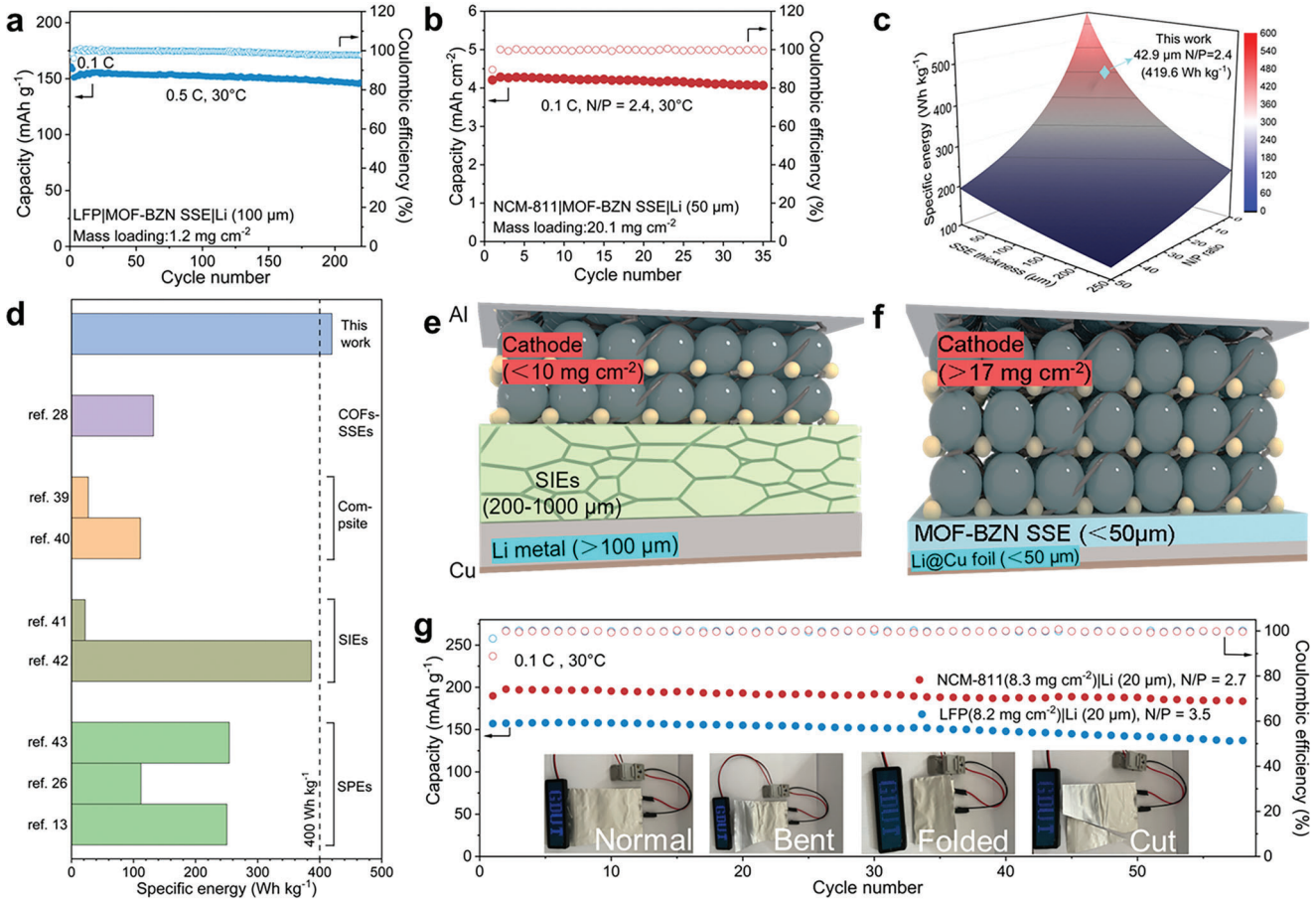

Figure 5. Toward a high-energy solid-state battery (SSB) with metal-organic framework with customized bilayer zwitterionic nanochannels (MOF-BZN) solid-state electrolyte (SSE). a) Cycling performance of LFP|MOF-BZN SSE|Li full cell. b) Cycling performance of NCM-811|MOF-BZN SSE|Li full cell with high cathode loading. c) Estimated specific energy density of full cell as the factors of the thickness of SSE layers and N/P ratio in SSB using NCM-811 and Li foil. d) Comparison of SSBs specific energy based on different SSEs. Schematic illustration of SSBs based on conventional SSE (e) and MOF-BZN SSE (f). g) Cycling performances of LFP|MOF-BZN SSE|Li and NCM-811|MOF-BZN SSE|Li pouch cells. The insets show the images of pouch cell after being bent, folded, or cut off.

requirements and is thus highly qualified for being applied in solid-state LMBs.

To demonstrate the applicability of MOF-BZN SSE in SSBs, SSBs with LFP as model cathode were firstly assembled. As shown in Figure S31 (Supporting Information), the LFP|SSE|Li SSB exhibits specific discharge capacities of 160, 153, and 130 mAh g^{-1} at 0.1, 0.2, and 0.5 C, respectively. More importantly, benefiting from the high electrochemical stability, SSB assembled with MOF-BZN SSE has the potential to work under higher voltage. As indicated in Figure S32 (Supporting Information), the NCM-811|SSE|Li SSB can also work steadily with specific discharge capacities of 219, 192, and 175 mAh g^{-1} at 0.1, 0.2, and 0.5, respectively. Both the LFP|SSE|Li and the NCM-811|SSE|Li SSBs can stably work at 0.5 C for over 200 and 300 cycles, respectively (**Figure 5**a and Figure S33, Supporting Information).

To demonstrate the applicability of MOF-BZN SSE in high-energy SSBs, solid-state full cells were assembled with constrained conditions including both high-loading cathode and limited lithium source. As shown in Figure S34 (Supporting Information), the LFP|SSE|Li full cell with high-loading LFP (17.0 mg cm^{-2}) and a low N/P ratio of 3.8 delivered areal capacity of 2.7 mAh cm^{-2} at 0.1 C and can work steadily at 30 °C, rendering a high specific energy of 259.2 Wh $kg_{anode+cathode+electrolyte}^{-1}$. As shown in Figure 5b,c and Table S2 (Supporting Information), the NCM-811|MOF-BZN SSE|Li full cell with high-loading NCM-811 of 20.1 mg cm^{-2} and low N/P ratio of 2.4 enables stable working at 30 °C with an areal capacity of 4.3 mAh cm^{-2} at 0.1 C, leading to a high specific energy of 419.6 Wh $kg_{anode+cathode+electrolyte}^{-1}$ (742 Wh $kg_{NCM-811}^{-1}$). This presents a highly competitive specific energy among the previously reported cells using SPEs, SIEs, composite SSEs, and COF SSEs (Figure 5d and Table S3, Supporting Information).[13,26,28,40–44] The high specific energies of the MOF-BZN SSE full cells can be attributed to the light weight of the thin Li metal anode, thin MOF-BZN SSE, and high-loading cathode that replace the excessive Li metal anode, thick SIEs, and low-loading cathode typically used in SSBs (Figure 5e,f). The specific energy of solid-state LMBs at ambient temperature was calculated based on the weight of the anode, cathode, and solid electrolyte.

As MOF-BZN SSE has shown excellent flexibility, a foldable solid-state pouch cell with limited lithium metal source (N/P ratio = 3.8) was then fabricated (Figure S35, Supporting Information). The SSE was rolled directly on the cathode to enhance the contact between cathode and SSE, which is crucial for optimizing the ion transport across interface. Figure 5g shows the cyclic performance of LFP|MOF-BZN SSE|Li and NCM-811|MOF-BZN SSE|Li pouch-type cells at 0.1 C, respectively, which also show a high capacity and charge/discharge platforms similarly to those of the coin-type cells (Figure S34, Supporting Information and Figure 5b). More importantly, the foldable solid-state pouch cell can remain operational in various folded states and even after being cut.

3. Conclusion

An exceptional MOF SSE with excellent comprehensive performance has been realized via constructing BZN in MOFs. The elaborated MOF-BZN SSE incorporates BZN, enabling selective superionic conduction while exhibiting remarkable capabilities for Li^+ transport, a wide electrochemical window, physical flexibility, chemical stability, and fire resistance. Furthermore, MOF-BZN enables stable operation of high-energy solid-state full cells even under controlled N/P ratio and high cathode loading, rendering high specific energy of 419.6 Wh kg^{-1} of electrodes plus electrolyte. This strategy of constructing bilayer zwitterionic MOFs is universal and therefore is expected to pave the way for developing new-type SSEs based on porous materials through multiple engineering techniques. More importantly, the SSEs developed using this strategy hold great promise for a wide range of solid-state rechargeable batteries including metal-air batteries, metal-sulfur batteries, and various metal ions batteries.

4. Experimental Section

The Experimental Section is available in the Supporting Information.

Supporting Information

Supporting Information is available from the Wiley Online Library or from the author.

Acknowledgements

Y.O. and W.G. contributed equally to this work. The authors gratefully acknowledge financial support from the National Natural Science Foundation of China (Nos. 51920105004, 51902060, and 52090021) and the Natural Science Foundation of Guangzhou, China (2023A04J1602). The authors would also like to thank the Analysis and Test Center of Guangdong University for the tests.

Conflict of Interest

The authors declare no conflict of interest.

Data Availability Statement

The data that support the findings of this study are available from the corresponding author upon reasonable request.

Keywords

all-solid-state batteries, bilayer zwitterionic nanochannels, ion conduction, metal-organic frameworks, solid-state electrolytes

Received: May 17, 2023
Revised: June 14, 2023
Published online: July 28, 2023

[1] L. Z. Fan, H. He, C. W. Nan, *Nat. Rev. Mater.* **2021**, *6*, 1003.
[2] Y. Liu, X. Tao, Y. Wang, C. Jiang, C. Ma, O. Sheng, G. Lu, W. Lou Xiong, *Science* **2022**, *375*, 739.
[3] R. Chen, Q. Li, X. Yu, L. Chen, H. Li, *Chem. Rev.* **2020**, *120*, 6820.
[4] Y. Xiao, S. Guo, Y. Ouyang, D. Li, X. Li, W. He, H. Deng, W. Gong, C. Tan, Q. Zeng, Q. Zhang, S. Huang, *ACS Nano* **2021**, *15*, 18363.
[5] Q. Zeng, X. Li, W. Gong, S. Guo, Y. Ouyang, D. Li, Y. Xiao, C. Tan, L. Xie, H. Lu, Q. Zhang, S. Huang, *Adv. Energy Mater.* **2022**, *12*, 2104074.
[6] M. Li, C. Wang, Z. Chen, K. Xu, J. Lu, *Chem. Rev.* **2020**, *120*, 6783.
[7] R. S. Longchamps, X. G. Yang, C. Y. Wang, *ACS Energy Lett.* **2022**, *7*, 1103.
[8] C. Y. Wang, T. Liu, X. G. Yang, S. Ge, N. V. Stanley, E. S. Rountree, Y. Leng, B. D. McCarthy, *Nature* **2022**, *611*, 485.
[9] J. Ma, G. Zhong, P. Shi, Y. Wei, K. Li, L. Chen, X. Hao, Q. Li, K. Yang, C. Wang, W. Lv, Q. Yang, Y. He, F. Kang, *Energy Environ. Sci.* **2022**, *15*, 1503.
[10] R. Zhao, Y. Wu, Z. Liang, L. Gao, W. Xia, Y. Zhao, R. Zou, *Energy Environ. Sci.* **2020**, *13*, 2386.
[11] X. Feng, H. Fang, N. Wu, P. Liu, P. Jena, J. Nanda, D. Mitlin, *Joule* **2022**, *6*, 543.
[12] Y. Li, M. Karimi, Y. Gong, N. Dai, V. Safarifard, H. Jiang, *Matter* **2021**, *4*, 2230.
[13] C. Yang, Q. Wu, W. Xie, X. Zhang, A. Brozena, J. Zheng, M. N. Garaga, B. H. Ko, Y. Mao, S. He, Y. Gao, P. Wang, M. Tyagi, F. Jiao, R. Briber, P. Albertus, C. Wang, S. Greenbaum, Y. Hu, A. Isogai, M. Winter, K. Xu, Y. Qi, L. Hu, *Nature* **2021**, *598*, 590.
[14] S. J. Tan, W. P. Wang, Y. F. Tian, S. Xin, Y. G. Guo, *Adv. Funct. Mater.* **2021**, *31*, 2105253.
[15] J. Wu, S. Liu, F. Han, X. Yao, C. Wang, *Adv. Mater.* **2021**, *33*, 2000751.
[16] C. Wang, J. Liang, Y. Zhao, M. Zheng, X. Li, X. Sun, *Energy Environ. Sci.* **2021**, *14*, 2577.
[17] J. Wu, L. Yuan, W. Zhang, Z. Li, X. Xie, Y. Huang, *Energy Environ. Sci.* **2021**, *14*, 12.
[18] S. Dai, A. Tissot, C. Serre, *Adv. Energy Mater.* **2022**, *12*, 2100061.
[19] G. Cai, P. Yan, L. Zhang, H. C. Zhou, H. L. Jiang, *Chem. Rev.* **2021**, *121*, 12278.
[20] Z. Chang, H. Yang, X. Zhu, P. He, H. Zhou, *Nat. Commun.* **2022**, *13*, 1510.
[21] T. Hou, W. Xu, X. Pei, L. Jiang, O. M. Yaghi, K. A. Persson, *J. Am. Chem. Soc.* **2022**, *144*, 13446.
[22] J. Jie, Y. Liu, L. Cong, B. Zhang, W. Lu, X. Zhang, J. Liu, H. Xie, L. Sun, *J. Energy Chem.* **2020**, *49*, 80.
[23] Z. Wang, R. Tan, H. Wang, L. Yang, J. Hu, H. Chen, F. Pan, *Adv. Mater.* **2018**, *30*, 1704436.
[24] S. Liu, L. Zhou, J. Han, K. Wen, S. Guan, C. Xue, Z. Zhang, B. Xu, Y. Lin, Y. Shen, L. Li, C. W. Nan, *Adv. Energy Mater.* **2022**, *12*, 2200660.
[25] Y. Yan, J. Ju, S. Dong, Y. Wang, L. Huang, L. Cui, F. Jiang, Q. Wang, Y. Zhang, G. Cui, *Adv. Sci.* **2021**, *8*, 2003887.
[26] J. Wan, J. Xie, X. Kong, Z. Liu, K. Liu, F. Shi, A. Pei, H. Chen, W. Chen, J. Chen, X. Zhang, L. Zong, J. Wang, L. Chen, J. Qin, Y. Cui, *Nat. Nanotechnol.* **2019**, *14*, 705.

[27] X. Li, Q. Hou, W. Huang, H. Xu, X. Wang, W. Yu, R. Li, K. Zhang, L. Wang, Z. Chen, K. Xie, K. P. Loh, *ACS Energy Lett.* **2020**, *5*, 3498.
[28] D. Guo, D. B. Shinde, W. Shin, E. A. Hamad, A.-H. Emwas, Z. Lai, A. Manthiram, *Adv. Mater.* **2022**, *34*, 2201410.
[29] C. Niu, W. Luo, C. Dai, C. Yu, Y. Xu, *Angew. Chem., Int. Ed.* **2021**, *60*, 24915.
[30] K. Jeong, S. Park, G. Y. Jung, S. H. Kim, Y. H. Lee, S. K. Kwak, S. Y. Lee, *J. Am. Chem. Soc.* **2019**, *141*, 5880.
[31] Z. Li, Z. Liu, Z. Mu, C. Cao, Z. Li, T. Wang, Y. Li, X. Ding, B. Han, W. Feng, *Mater. Chem. Front.* **2020**, *4*, 1164.
[32] X. Liu, J. Liu, B. Lin, F. Chu, Y. Ren, *ACS Appl. Energy Mater.* **2022**, *5*, 1031.
[33] J. F. Wu, X. Guo, *J. Mater. Chem. A* **2019**, *7*, 2653.
[34] M. Balaish, J. C. Gonzalez-Rosillo, K. J. Kim, Y. Zhu, Z. D. Hood, J. L. M. Rupp, *Nat. Energy* **2021**, *6*, 227.
[35] Y. Zhu, Y. Mo, *Angew. Chem., Int. Ed.* **2020**, *59*, 17472.
[36] P. Lu, L. Liu, S. Wang, J. Xu, J. Peng, W. Yan, Q. Wang, H. Li, L. Chen, F. Wu, *Adv. Mater.* **2021**, *33*, 2100921.
[37] C. Wang, K. Fu, S. P. Kammampata, D. W. McOwen, A. J. Samson, L. Zhang, G. T. Hitz, A. M. Nolan, E. D. Wachsman, Y. Mo, V. Thangadurai, L. Hu, *Chem. Rev.* **2020**, *120*, 4257.
[38] J. Wan, J. Xie, X. Kong, Z. Liu, K. Liu, F. Shi, A. Pei, H. Chen, W. Chen, J. Chen, X. Zhang, L. Zong, J. Wang, L. Q. Chen, J. Qin, Y. Cui, *Nat. Nanotechnol.* **2019**, *14*, 705.
[39] X. Wang, C. Zhang, M. Sawczyk, J. Sun, Q. Yuan, F. Chen, T. C. Mendes, P. C. Howlett, C. Fu, Y. Wang, X. Tan, D. J. Searles, P. Král, C. J. Hawker, A. K. Whittaker, M. Forsyth, *Nat. Mater.* **2022**, *21*, 1057.
[40] J. Sun, C. He, X. Yao, A. Song, Y. Li, Q. Zhang, C. Hou, Q. Shi, H. Wang, *Adv. Funct. Mater.* **2021**, *31*, 2006381.
[41] H. Duan, M. Fan, W. Chen, J. Li, P. Wang, W. Wang, J. Shi, Y. Yin, L. Wan, Y. Guo, *Adv. Mater.* **2019**, *31*, 1807789.
[42] L. Ye, X. Li, *Nature* **2021**, *593*, 218.
[43] Y. G. Lee, S. Fujiki, C. Jung, N. Suzuki, N. Yashiro, R. Omoda, D.-S. Ko, T. Shiratsuchi, T. Sugimoto, S. Ryu, J. H. Ku, T. Watanabe, Y. Park, Y. Aihara, D. Im, I. T. Han, *Nat. Energy* **2020**, *5*, 299.
[44] Q. Zhao, X. Liu, S. Stalin, K. Khan, L. A. Archer, *Nat. Energy* **2019**, *4*, 365.